remote sensing

MDPI

Article

Improving the Gross Primary Productivity Estimation by Simulating the Maximum Carboxylation Rate of Maize Using Leaf Age

Xin Zhang, Shuai Wang, Weishu Wang, Yao Rong, Chenglong Zhang, Chaozi Wang and Zailin Huo *

Center for Agricultural Water Research in China, China Agricultural University, Beijing 100083, China; b20203090640@cau.edu.cn (X.Z.); wangshuaiszo@163.com (S.W.); wws0208@cau.edu.cn (W.W.); s20193091608@cau.edu.cn (Y.R.); zhangcl1992@cau.edu.cn (C.Z.); chaoziwang@cau.edu.cn (C.W.)
* Correspondence: huozl@cau.edu.cn

Abstract: Although the maximum carboxylation rate (V_{cmax}) is an important parameter to calculate the photosynthesis rate for the terrestrial biosphere models (TBMs), current models could not satisfactorily estimate the V_{cmax} of a crop because the V_{cmax} is always changing during crop growth period. In this study, the Breathing Earth System Simulator (BESS) and light response curve (LRC) were combined to invert the time-continuous V_{m25} (V_{cmax} normalized to 25 °C) using eddy covariance measurements and remote sensing data in five maize sites. Based on the inversion results, we propose a Two-stage linear model using leaf age to estimate crop V_{m25}. The leaf age can be readily calculated from the date of emergence, which is usually recorded or can be readily calculated from the leaf area index (LAI), which can be readily obtained from high spatiotemporal resolution remote sensing images. The V_{m25} used to calibrate and validate our model was inversely solved by combining the BESS and LRC and using eddy covariance measurements and remote sensing data in five maize sites. Our Two-stage linear model (R^2 = 0.71–0.88, RMSE = 5.40–7.54 μmol m^{-2} s^{-1}) performed better than the original BESS (R^2 = 0.01–0.67, RMSE = 13.25–18.93 μmol m^{-2} s^{-1}) at capturing the seasonal variation in the V_{m25} of all of the five maize sites. Our Two-stage linear model can also significantly improve the accuracy of maize gross primary productivity (GPP) at all of the five sites. The GPP estimated using our Two-stage linear model (underestimated by 0.85% on average) is significantly better than that estimated by the original BESS model (underestimated by 12.60% on average). Overall, our main contributions are as follows: (1) by using the BESS model instead of the BEPS model coupled with the LRC, the inversion of V_{m25} took into account the photosynthesis process of C4 plants; (2) the maximum value of V_{m25} (i.e., PeakV_{m25}) during the growth and development of maize was calibrated; and (3) by using leaf age as a predictor of V_{m25}, we proposed a Two-stage linear model to calculate V_{m25}, which improved the estimation accuracy of GPP.

Keywords: maximum carboxylation rate (V_{cmax}); gross primary productivity (GPP); breathing earth system simulator (BESS); light response curve (LRC); leaf age

Citation: Zhang, X.; Wang, S.; Wang, W.; Rong, Y.; Zhang, C.; Wang, C.; Huo, Z. Improving the Gross Primary Productivity Estimation by Simulating the Maximum Carboxylation Rate of Maize Using Leaf Age. *Remote Sens.* **2024**, *16*, 2747. https://doi.org/10.3390/rs16152747

Academic Editors: Thomas Alexandridis, Mavromatis Theodoros and Vassilis Aschonitis

Received: 1 June 2024
Revised: 21 July 2024
Accepted: 25 July 2024
Published: 27 July 2024

1. Introduction

Gross primary productivity (GPP) refers to the carbon dioxide fixed by plants through photosynthesis, constituting the largest carbon exchange between terrestrial ecosystems and the atmosphere [1]. GPP plays a crucial role in regulating the terrestrial carbon budget, thus exerting a significant impact on climate change [2–5]. Croplands exhibit high primary productivity during the growing season, underscoring the importance of accurately characterizing crop physiology throughout the growing seasons to predict carbon exchange in agricultural systems [6,7]. Process-based models, such as terrestrial biosphere models (TBMs), are widely employed for estimating GPP at both regional and global scales [8–10]. These models typically incorporate photosynthesis modules based on photosynthesis models [11,12]. Central to these photosynthesis models is the parameter

known as the maximum carboxylation rate (V_{cmax}), which characterizes the potential photosynthetic capacity of leaves [11,13]. Consequently, the accurate estimation of the V_{cmax} is paramount for enhancing the accuracy and performance of TBMs [14].

V_{cmax} fluctuates abruptly during the crop growth period; thus, taking the variation in V_{cmax} into account is crucial for accurately calculating GPP in models [15–17]. However, V_{cmax} cannot be directly measured, and it must be inferred from leaf gas exchange measurement, which is time-consuming, resulting in limited data availability across a wide range of conditions [18]. In most TBMs, V_{cmax} is assumed to be a fixed value (normalized to 25 °C, V_{m25}) based on plant functional type, disregarding temporal and spatial variations in V_{m25} [7,19–22]. This assumption inevitably introduces significant bias in simulated photosynthesis, particularly in regions characterized by substantial seasonal fluctuations [15,23]. To minimize the bias, temporal variations in V_{m25} are modeled by establishing relationships between V_{m25} and more readily available plant traits [18,24]. Some studies have inverted V_{m25} using eddy covariance measurements and remote sensing data [25–30]. Yuan used the ensemble Kalman filter (EnKF) to obtain the temporal variation in the V_{m25} of maize [17]. Zheng and Xie inverted the time series of V_{m25} by coupling Boreal Ecosystem Productivity Simulator (BEPS) and light response curve (LRC) based on eddy covariance observations in flux sites [31,32]. The results indicated that this approach can effectively optimize V_{m25}, but it has only been applied to C3 plants, and its applicability to C4 plants has not been studied yet [31–33].

Despite technological advances in deriving V_{m25}, modeling V_{m25} through plant traits remains challenging. Advances in remote sensing and hyperspectral imaging technology have proven useful for estimating photosynthetic capacity across large spatial and temporal scales [18,34–38]. The strong correlation between the leaf nitrogen content (N_{Leaf}) and V_{m25} has garnered significant attention [39–41]. However, obtaining accurate N_{Leaf} through remote sensing data remains a challenge, which impedes the use of leaf nitrogen to parameterize V_{m25} [8,24]. Chlorophyll plays a crucial role in photosynthesis by capturing photons and providing the biochemical energy necessary for carbon fixation reactions [42]. Since N_{Leaf} includes both photosynthetic and non-photosynthetic components, some researchers argue that leaf chlorophyll content (Chll) is a more accurate indicator of V_{m25} than N_{Leaf} content [24,43]. Houborg summarized the semi-empirical relationship between Chll and V_{m25} [19]. By parameterizing this relationship, it has been successfully applied to a variety of crops [18,44,45]. The practical limitation of using Chll to parameterize V_{m25} at large spatial scales has been the lack of accurate remote sensing Chll products at regional or global scales. The Sentinel-2A satellite, launched in 2015, and the Sentinel-2B satellite, launched in 2017, carry multispectral imagers (MSIs) with red-edge bands sensitive to Chll and offer high temporal and spatial resolution. However, estimating Chll relies on complex models that typically require ground validation data for calibration [24,46]. The availability of the satellite observations of sun-induced fluorescence (SIF) offers a new perspective for monitoring crop V_{m25} [19,20]. Chlorophyll fluorescence is widely regarded as a direct proxy for electron transport and, consequently, photosynthesis [47,48]. Studies have demonstrated a strong connection between SIF and V_{m25}, indicating that SIF could be helpful for improving the accuracy of V_{m25} estimations at large spatial scales [42,49,50]. However, although SIF is effective and remote sensing products with 500–5000 m resolution are available, such as CSIF and GOSIF, the resolution of current SIF products is still relatively low compared to other vegetation parameter products, which can achieve a resolution of 30 m or higher [51]. The vegetation canopy structure directly influences various physical and biological processes, such as radiative transfer and photosynthesis [52]. Thus, in recent years, vegetation indices (VIs) have been employed to empirically estimate V_{m25} [53]. Muraoka, et al. [54] divided the growth period into two stages and established distinct relationships between VIs and canopy-level V_{m25} for each stage. However, Zhou highlighted that the relationship between traditional VIs and V_{m25} was not universal across different sites [55]. LAI is a VI commonly used to characterize seasonal changes in V_{m25} [56]. However, it is commonly observed that photosynthesis peaks earlier than the canopy structure indices [57].

Leaf age has been found to be well correlated with V_{m25} and substantial evidence indicates biochemical differences between young and old leaves [58,59]. Recent studies have demonstrated that leaf age plays a crucial role in determining photosynthetic rates [60–62], with V_{m25} exhibiting notable changes with the aging of leaves [8,16,63–65]. Generally, it is observed that the V_{m25} of newly mature leaves tends to be higher compared to that of younger and older leaves [66]. As leaves undergo senescence, Rubisco gradually becomes inactivated, the electron transport rate decreases, and enzymes are deactivated. Consequently, both the rates of photosynthesis and respiration decline with leaf aging [58,59,67]. It is worth noting that most of the research on the relationship between V_{m25} and leaf age has focused on trees [24,66], and there has been limited investigation into this relationship in crops [58,59,68]. Miner and Bauerle analyzed the seasonal changes in V_{m25} for maize and sunflower through gas exchange experiments [6]. The study revealed that the V_{m25} of maize decreases in a nearly linear trend from the mid-vegetative stage to the late senescence stage. For sunflowers, V_{m25} remained relatively stable from the late vegetative stage to the early reproductive stage, then significantly decreased in the late reproductive stage. Li found that rice V_{m25} exhibited a trend similar to leaf age under different experimental conditions and emphasized that a general formula for V_{m25} changes with leaf age has not yet been established [65].

Despite the well-known, strong correlation between leaf age and V_{m25} in crops, to our knowledge, this relationship has not yet been quantified. Therefore, the objectives of our study are (1) to derive time-continuous V_{m25} for maize at five sites by considering the photosynthesis process of C4 plants; (2) to calibrate the maximum value of V_{m25} (i.e., $PeakV_{m25}$) during the growing season of maize based on the inverted V_{m25}; and (3) to propose a Two-stage linear model that leverages leaf age to improve the accuracy of V_{m25} and GPP estimation.

2. Data Availability

2.1. Eddy Covariance Data

Hourly or half-hourly GPP data obtained by eddy covariance (EC) observations were used to estimate V_{m25} in five flux sites located in maize fields in United States and in China (Table 1). The hourly GPP data for the US-Ne1, US-Ne2, and US-Ne3 were obtained from the FLUXNET2015 database [69]. The US-Ne1 site was always planted with maize, whereas the US-Ne2 and US-Ne3 sites were rotating, planted with maize and soybeans. The half-hourly GPP data for the Daman were acquired from the National Tibetan Plateau Data Center [70,71]. We obtained the half-hourly GPP data for the Fenzidi ourselves, from our own flux site in the Hetao Irrigation District, Inner Mongolia Autonomous Region, China. The air temperature (T), relative humidity (RH), wind speed (WS), atmosphere pressure (Pa), carbon dioxide concentration (Ca) and the incoming solar radiation (SR) were also provided by the five flux sites.

Table 1. Summary of flux sites information.

Site	Latitude	Longitude	Crop Type	Year	LAI
US-Ne1	41.165°N	96.477°W	Maize	2001–2012	—
US-Ne2	41.165°N	96.470°W	Maize–Soybean	2001–2012	Literature *
US-Ne3	41.180°N	96.440°W	Maize–Soybean	2001–2012	Literature *
Daman	38.853°N	100.376°E	Maize	2018, 2019, 2021	measured
Fenzidi	41.153°N	107.653°E	Maize	2017, 2018, 2020	measured

* the LAI data for the site were partially obtained from the literature [72].

2.2. Remote Sensing Data

The moderate-resolution imaging spectroradiometer (MODIS) surface reflectance data were obtained from MCD43A4.061. The reflectance values across all bands served as the input for the BESS model and for the calculation of LAI. It is worth noting that MODIS LAI tends to significantly underestimate crop LAI [73]. Measured LAI values were provided

for the Fenzidi and Daman sites, while LAI values for certain years at US-Ne2 and US-Ne3 were extracted from the literature [72]. To estimate LAI values for other years, a machine learning model (ExtraTreesRegressor) was employed, demonstrating strong simulation performance (R^2 = 0.94) (Figure A1).

The clumping index (Ω) is another vegetation canopy structure index, quantifying the degree of deviation in leaf spatial distribution from a random pattern in BESS [74,75]. The Ω values were estimated using the MODIS BRDF product at a resolution of 500 m [76,77]. Ω values range from 0 to 1, where 1 indicates a randomly distributed canopy. Smaller Ω values indicate a more clustered canopy structure.

3. Method

Our approach is depicted in Figure 1. Firstly, the BESS model and LRC were combined to derive the time-continuous V_{m25}. The BESS model distinguishes the PAR absorbed by the sunlit leaves and shaded leaves. By integrating the BESS model and LRC, canopy GPP is separated into contributions from sunlit and shaded leaves. V_{cmax} is inverted utilizing Collatz's model based on the GPP from sunlit leaves, and then normalized to V_{m25} using a temperature function (Section 3.1). Next, the Two-stage linear model was employed to simulate V_{m25} based on leaf age (Section 3.2). Finally, V_{m25} was simulated using our Two-stage model and validated against the inverted V_{m25}, with further verification through GPP simulation results (Section 3.3).

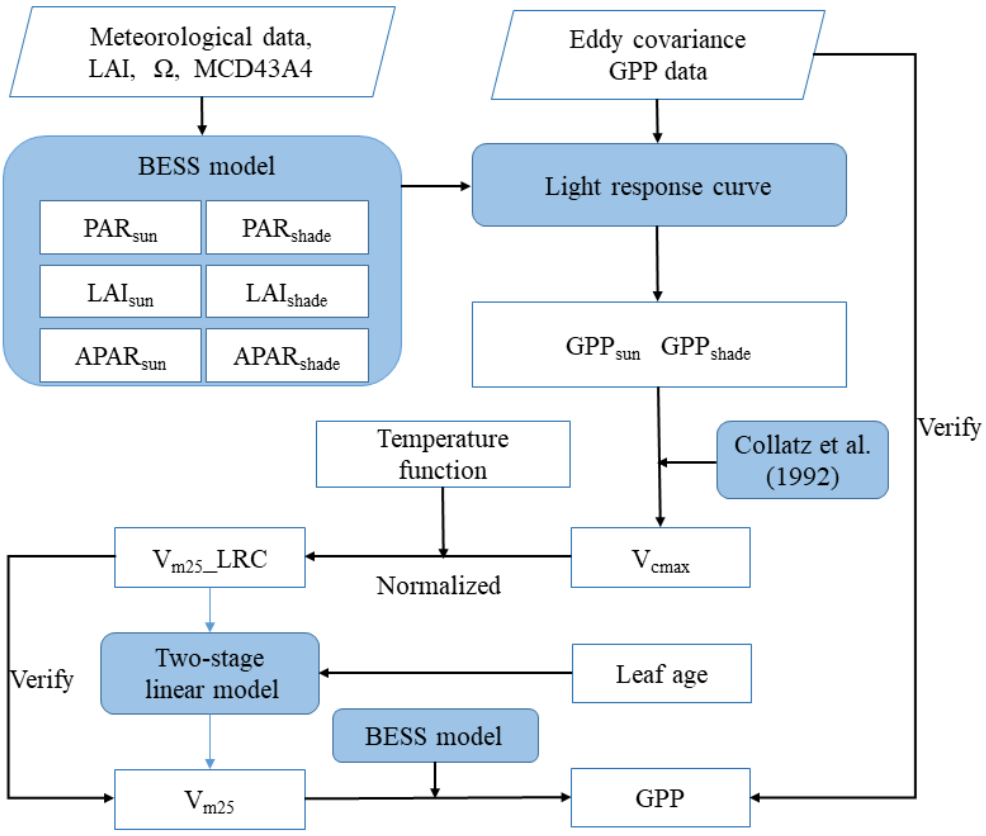

Figure 1. The process of inverting V_{m25} through coupling BESS and LRC with eddy covariance measurements and remotely sensed data, and the validation of the proposed Two-stage linear model [12].

3.1. Inversely Solving V_{m25} by Coupling the BESS and LRC

Zheng and Xie inverted the time series of V_{m25} by coupling Boreal Ecosystem Productivity Simulator (BEPS) with light response curve (LRC), utilizing EC observations data and remote sensing data from flux sites [31,32]. This method effectively optimizes V_{m25} by

separating the contributions of sunlit leaves and shade leaves. However, the BEPS model does not account for the physiological process for C4 plants, such as maize [33]. What is more, BEPS employs a fixed V_{m25} value. The Breathing Earth System Simulator (BESS) model not only differentiates between sunlit and shaded leaves [56], but also distinguishes between C3 and C4 plants. Additionally, BESS incorporates LAI to account for seasonal variation in V_{m25}. Therefore, we substituted the BEPS model with the BESS model.

3.1.1. The Separation of Sunlit and Shaded GPP by BESS

In the BESS model, the photosynthesis rate at leaf-level is calculated by Farquhar's and Collatz's model [11,12], while a "two-leaf" canopy model is employed to upscale the leaf-level photosynthesis rate to canopy GPP. The total GPP of the canopy is determined by summing the contributions from sunlit leaves and shaded leaves as follows:

$$GPP = GPP_{sun} + GPP_{shade} \quad (1)$$

where GPP_{sun} and GPP_{shade} are the GPP of sunlit and shaded leaves, respectively. GPP can be calculated from photosynthesis rate and the corresponding LAI; therefore, Equation (1) can be expressed as:

$$GPP = A_{sun}LAI_{sun} + A_{shade}LAI_{shade} \quad (2)$$

where A_{sun} and A_{shade} are the photosynthesis rates per units of sunlit and shaded leaves, respectively; LAI_{sun} and LAI_{shade} are the LAI of sunlit and shaded leaves, which can be calculated by:

$$LAI_{sun} = 2\cos\theta\left(1 - \exp\left(-\frac{0.5\Omega LAI}{\cos\theta}\right)\right) \quad (3)$$

$$LAI_{shade} = LAI - LAI_{sun} \quad (4)$$

where θ is solar zenith angle, Ω is the clumping index, and LAI is the leaf area index of the whole canopy.

3.1.2. Photosynthesis Rates of Sunlit and Shaded Leaves Estimated by LRC

Light response curve is a commonly utilized tool to depict the correlation between the photosynthetic rate and photosynthetically active radiation (PAR). The rectangular hyperbola is employed to characterize the shape of the light response curve [78]:

$$A = \frac{\alpha IP}{\alpha I + P} \quad (5)$$

where A is the gross photosynthesis rate; α is the maximum light use efficiency (LUE) obtained by the initial slope of the curve; I is the absorbed photosynthetically active radiation (APAR) of the leaf per unit; P is the gross photosynthetic rate under saturated radiation.

The light response curves are employed to estimate A_{sun} and A_{shade}, respectively [31,33]. Then, the total canopy GPP of Equation (2) can be expressed as:

$$GPP = LAI_{sun}\frac{\alpha I_{sun}P_{sun}}{\alpha I_{sun} + P_{sun}} + LAI_{shade}\frac{\alpha I_{shade}P_{shade}}{\alpha I_{shade} + P_{shade}} \quad (6)$$

where I_{sun} and I_{shade} are PAR absorbed by sunlit leaves and shade leaves ($APAR_{Sun}$ and $APAR_{Sh}$), respectively, and are calculated using the two-leaf canopy radiative transfer model in BESS (Appendix B); and P_{sun} and P_{shade} are given by:

$$P_{sun} = \frac{P_0 k\left(1 - e^{-kLAI - k_n LAI}\right)}{(k + k_n) \times \left(1 - e^{kLAI}\right)} \quad (7)$$

$$P_{shade} = \frac{P_0\left(\left(2\cos\theta k_n k - (k_n + k)e^{kLAI}\right)e^{-kLAI - k_k LAI} - \left((2\cos\theta k_n - 1)k - k_n\right)\right)}{\left(k_n^2 + k_n k\right)\left(LAI - 2\cos\theta\left(1 - e^{-kLAI}\right)\right)} \quad (8)$$

where P_0 is P on the top of the canopy; k_n describes the rate at which leaf nitrogen content decreases with increasing depth into the canopy, and is taken as 0.3 following the previous study [21].

$$k = \frac{0.5\Omega}{\cos\theta} \tag{9}$$

Here, α and P_o represent the two unknown parameters, both of which are contingent on the biological conditions of the leaves. During periods of low incoming radiation, such as in the morning or afternoon, the photosynthetic rate is presumed to be primarily influenced by radiation, leading to the maximum LUE at these times. To determine α for the day, GPP data are selected with incoming PAR less than 350 μmol $m^{-2}s^{-1}$ for regression analysis against APAR. The resulting slope of this regression is considered as α for the given day. The daily value of P_0 is then obtained through the optimization of eddy covariance GPP data after determining α.

3.1.3. The Inversion of V_{cmax} from Sunlit GPP

According to Collatz's model:

$$A = \min(A_j, A_c) - R_d \tag{10}$$

where A is the gross photosynthesis; A_j represents the rate of photosynthesis limited by radiation and A_c represents the rate of photosynthesis restricted by Rubisco; R_d is the rate of dark respiration.

When estimating V_{cmax} through the reversal of Collatz's method, it is essential that the photosynthetic rate is limited by V_{cmax}, rather than radiation. In shaded leaves, the photosynthetic rate is primarily regulated by radiation. Conversely, sunlit leaves receive more radiation than shaded leaves; thus, their photosynthetic rate is not controlled by radiation but by V_{cmax} when incident radiation levels are high. The separation of sunlit and shaded leaves enables the inversion of V_{cmax} from the GPP of sunlit leaves. For sunlit leaves, when incident radiation levels are low, such as in the early morning, the photosynthetic rate is dependent on radiation. However, as incident radiation increases, it gradually becomes limited by Rubisco. A threshold of 900 μmol $m^{-2}s^{-1}$ is utilized for radiation levels. When APAR exceeds this threshold, the photosynthetic rate is predominantly limited by V_{cmax}. Consequently, V_{cmax} is derived from the GPP of sunlit leaves under such conditions [31].

Once the GPP of sunlit leaves has been separated, the photosynthesis rate of sunlit leaves can be calculated as:

$$A_c = \frac{GPP_{sun}}{LAI_{sun}} \tag{11}$$

For C4 plants, according to Collatz's model [12], when the CO_2 fixation is controlled only by Rubisco, V_{cmax} is calculated as:

$$V_{cmax} = A_c \tag{12}$$

3.1.4. Normalizing V_{cmax} to 25 °C

The inverted V_{cmax} can be normalized to 25 °C (V_{m25}) using the temperature function [79]:

$$V_{m25} = \frac{V_{cmax}}{f(T)} \tag{13}$$

$$f(T) = \left(1 + \exp\left(\frac{(-220,000 + 710(T + 273))}{(R(T + 273))}\right)\right)^{-1} \tag{14}$$

where T is the leaf temperature; and R is the gas constant.

3.2. Two-Stage Linear Model

Crops typically experience rapid growth in the early stages, reaching a peak before gradually aging. Thus, we divided the crop growth period into an ascending phase and a

descending phase (Figure 2). According to FAO56 guidelines [80], the rapid growth period of maize typically spans from 35 to 50 days, counting from the date of emergence. Therefore, within this date range, we identified the day with the smallest change in LAI as the cut-off point between the ascending phase and descending phase, denoted as D_{Peak}. We discovered that V_{m25} exhibits a stronger correlation with leaf age than with LAI, particularly during the descending phase (Figure 2).

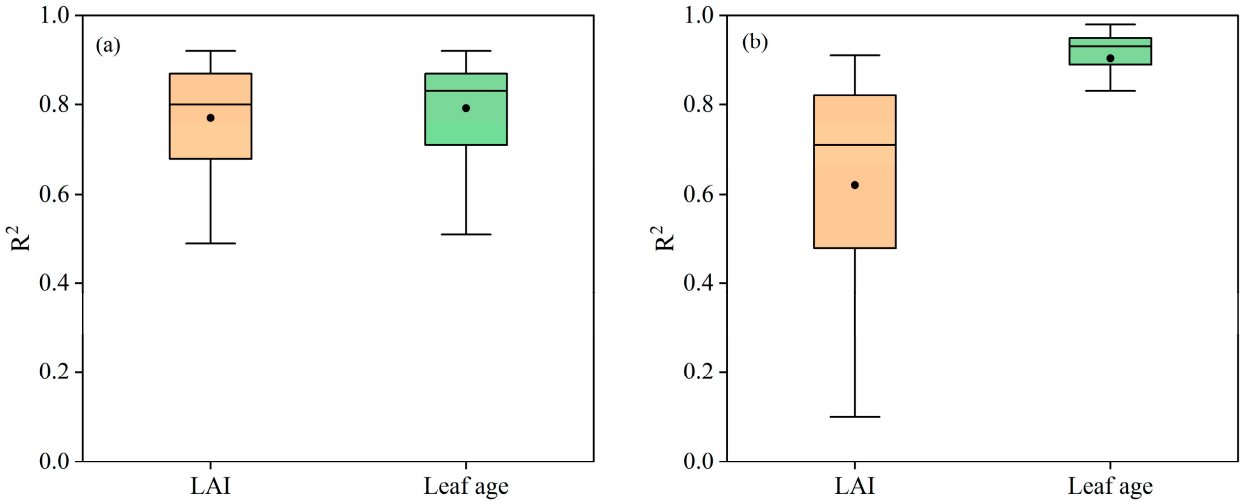

Figure 2. R^2 between V_{m25} and LAI, DOY during (**a**) the ascending stage and (**b**) the descending stage. QR indicate quartiles. The top and bottom boundaries of boxes indicate the values of the 25% percentile (QR1) and 75% percentile (QR3) values, respectively. The lines at both ends represent the maximum range (QR3 + 1.5 IQR) and the minimum range (QR1–1.5 IQR). The lines in the middle of the box represent the median, and the black diamonds represent the mean.

Building upon this discovery, we proposed a Two-stage linear model that utilizes leaf age to simulate V_{m25} (Figure 3). In this model, V_{m25} is linearly fitted separately for the ascending and descending phases (Equations (16) and (17)). Our Two-stage linear model is as follow:

$$V_{m25} = \begin{cases} k_1 \times D + V_{m25,ini} & , \quad D_{ini} < D < D_{Peak} \\ k_2 \times (D - D_{Peak}) & , \quad D_{peak} \leq D < D_{end} \end{cases} \tag{15}$$

where D_{ini} represents the leaf age when the crop initiates rapid growth, recorded as 0; D_{Peak} represents the leaf age when the V_{m25} reaches maximum; D_{end} denotes the ending leaf age of the crop growth period, typically when the GPP value observed by the flux sites approaches 0; and D represents the current leaf age. k_1 and k_2 denote the slopes of the ascending and descending stages of crop development, respectively.

$$k_1 = \frac{PeakV_{m25} - V_{m,ini}}{D_{Peak}} \tag{16}$$

$$k_2 = \frac{PeakV_{m25}}{D_{end} - D_{Peak}} \tag{17}$$

Leaf age is commonly used to describe the growth status and developmental stage of plants. Its specific definition and calculation methods can vary depending on the research objectives and plant species. In our study, leaf age refers to the physical age of the plant, meaning the actual time from emergence to the current leaf development stage, measured in days. The emergence dates for US-Ne1, US- Ne2, and US-Ne3 can be obtained from the literature. For the Daman and Fenzidi, the emergence dates can be inferred from the changing trends in LAI values.

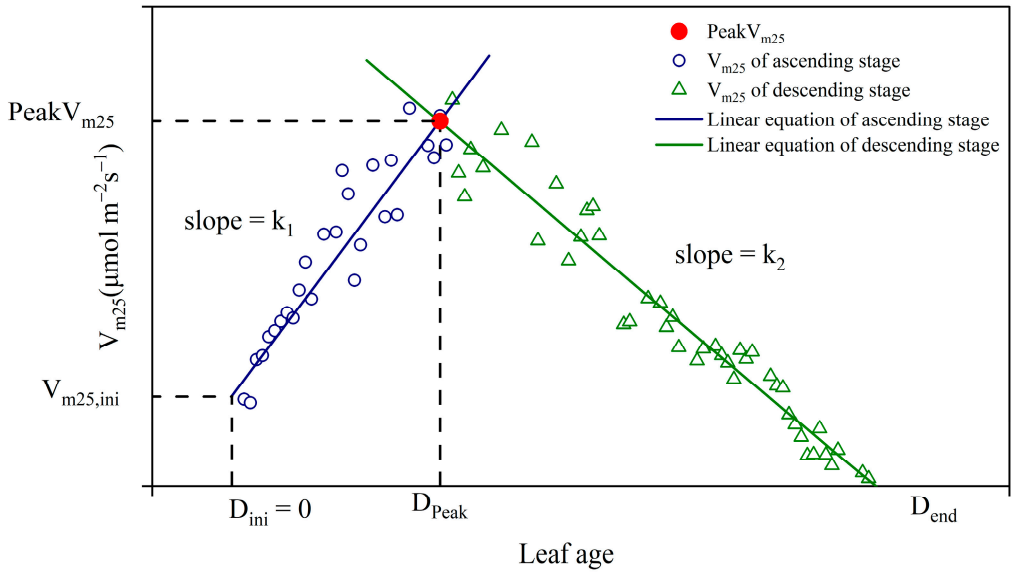

Figure 3. Schematic diagram of the Two-stage linear model.

3.3. Model Validation

3.3.1. Calibration and Validation of V_{m25}

Data from one-third of the years were utilized for calibrating the PeakV_{m25} (Section 3.2), while data from the remaining two-thirds of years were employed to validate the accuracy of the Two-stage linear model. It is worth mentioning that the estimation of V_{m25} for leaves operating under low radiation conditions is typically less accurate. The cumulative effect of errors in various underlying assumptions can lead to a relatively low signal-to-noise ratio [81]. Thus, V_{m25} values corresponding to low radiation were excluded.

The PeakV_{m25} was calculated for the three US sites (US-Ne1, US-Ne2, US-Ne3) and the two Chinese sites (Daman, Fenzidi) separately, to account for the difference in maize species. To determine the value of the PeakV_{m25}, data from the first third of each year at each site were selected. Linear regression between V_{m25} inverted by LRC and leaf age was performed for both the ascending phase and descending phase, respectively. The average PeakV_{m25} value for the first third years of the three US sites and the two Chinese sites are 65 and 38 μmol $m^{-2}s^{-1}$ (rounded to an integer), respectively. Note that $V_{m25,ini}$ is difficult to estimate when the GPP is close to zero or negative at the beginning of the growth period. Thus, the V_{m25} at the beginning of the growth period is set as 10 μmol $m^{-2}s^{-1}$, the median of the LRC inverted V_{m25} during this period (5–15 μmol $m^{-2}s^{-1}$).

3.3.2. Comparison with the V_{m25} Obtained by BESS

In the BESS model, seasonal variation in V_{m25} is taken into account [56,82]. It is assumed that the seasonal pattern of V_{m25} followed the seasonal pattern of LAI [83]. V_{m25} experiences a rapid increase during leaf development, reaching its peak in early leaf maturity, followed by a decline during senescence, irrespective of species. The date corresponding to the peak LAI value is identified, and the V_{m25} for that date was quantified (PeakV_{m25}). Subsequently, V_{m25} over the season is calculated as:

$$V_{m25} = V_{m25,min} + \frac{LAI}{LAI_{max}} \times (PeakV_{m25} - V_{m25,min}) \quad (18)$$

where LAI_{max} and LAI represent the maximum and current leaf area index, respectively, throughout the growing period. In the original BESS model, the PeakV_{m25} value of C4 crops was uniformly set as 33 μmol $m^{-2}s^{-1}$, without distinction among crop types. $V_{m25,min} = 0.3 \times PeakV_{m25}$.

In the original BESS model (Equation (18)), the PeakV_{m25} value of C4 crops was uniformly set at 33 μmol $m^{-2}s^{-1}$, without differentiation among crop species. In our model, the calibrated PeakV_{m25} value was substituted into the original BESS model to calculate V_{m25} (hereafter referred to as "BESS_P"), and then the performances of the original BESS, BESS_P and our Two-stage linear model in simulating V_{m25} were compared against the V_{m25} inversely solved by coupling the BESS and LRC using EC data.

3.3.3. Comparison with the GPP Obtained by BESS

Then, the original BESS model, BESS_P model, and the BESS model coupled with the Two-stage linear model (hereinafter referred to as "BESS_TL") were used to calculate GPP. These simulated GPP values were then compared with the GPP values measured at the flux sites to evaluate the performance of each model. This comparison helps in assessing the accuracy and reliability of each method in simulating GPP.

4. Results

4.1. Calibration and Validation of V_{m25}

To assess the performance of the Two-stage linear model (Equation (15)), the simulated V_{m25} was compared with the V_{m25} inversely solved by coupling the BESS and LRC using EC data (Figure 4, Table 2). Notably, the simulated V_{m25} aligns closely with that from LRC for both the calibration and validation samples at each site (Figure 4, Table 2). The performance of the Two-stage linear model was exceptional for the US-Ne2 and US-Ne3 sites, yielding R^2 values of 0.88 and 0.87, RMSE values of 6.82 μmol $m^{-2}s^{-1}$ for both, whereas the performance was not as good for Daman (R^2 = 0.71; RMSE = 6.44 μmol $m^{-2}s^{-1}$), due to the pronounced fluctuation in V_{m25} during the early stages of the growth period at Daman (Figure 5y, z).

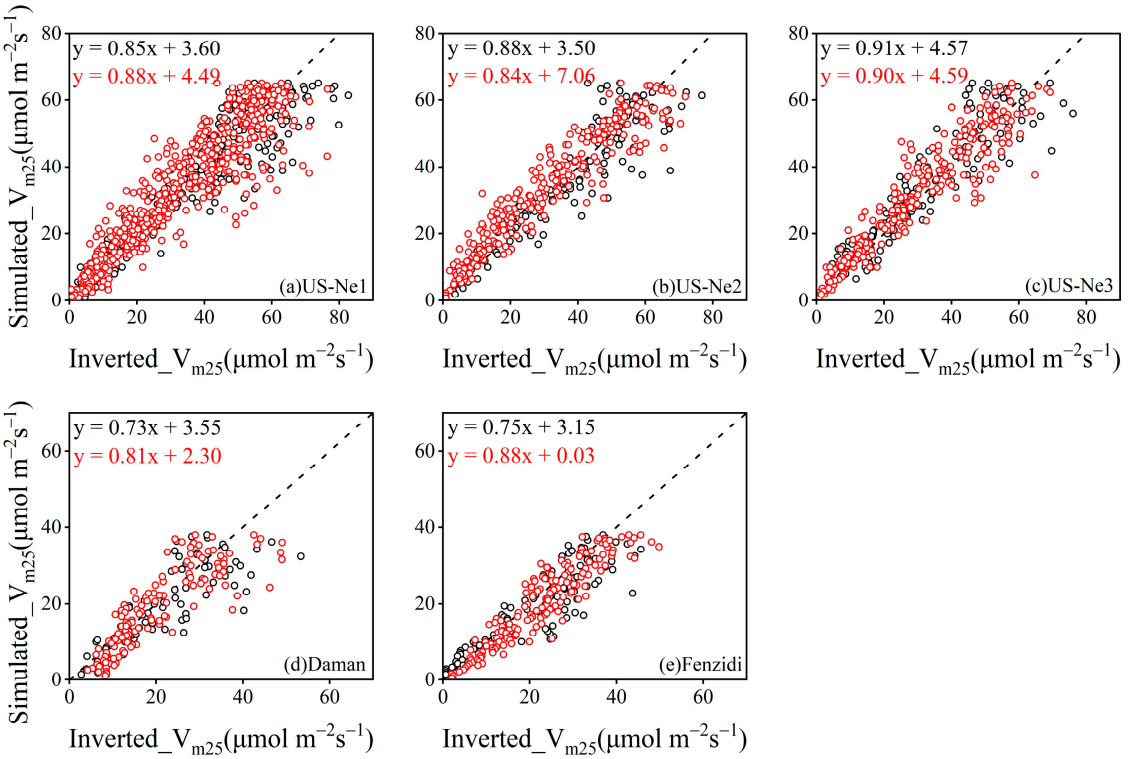

Figure 4. Comparing the V_{m25} simulated by the Two-stage linear model (Simulated_V_{m25}) and the V_{m25} inversely solved by coupling the BESS and LRC using EC data (Inverted_V_{m25}) at (**a**) US-Ne1, (**b**) US-Ne2, (**c**) US-Ne3, (**d**) Daman, (**e**) Fenzidi. Black dots represent values for the calibration data, red dots for the validation data.

Table 2. The performance of the original BESS, BESS_P and our Two-stage linear model at simulating the V_{m25} inversely solved by coupling the BESS and LRC using EC data at the five flux sites.

Site	BESS		BESS_P		BESS_TL	
	RMSE	R^2	RMSE	R^2	RMSE	R^2
US-Ne1	18.93	0.23	25.07	0.23	7.54	0.85
US-Ne2	16.58	0.52	22.67	0.52	6.82	0.88
US-Ne3	14.70	0.67	19.46	0.67	6.82	0.87
Daman	14.55	0.02	16.99	0.02	6.44	0.71
Fenzidi	13.25	0.01	15.30	0.01	5.40	0.82

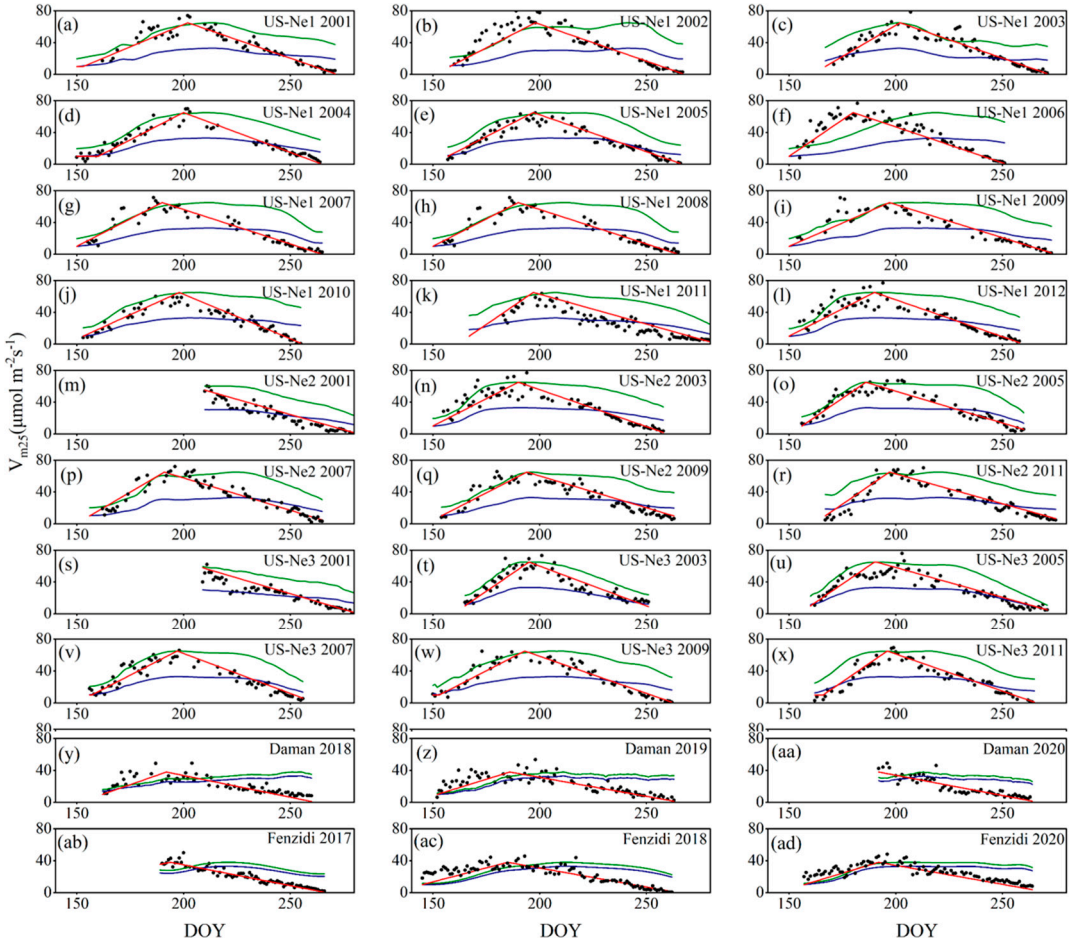

Figure 5. Comparison of V_{m25} calculated by BESS (blue lines), BESS_P (green lines) and our Two-stage linear model (red lines) in simulating the time series of V_{m25} inversely solved by coupling the BESS and LRC using EC data at the five flux sites: (**a**–**l**) show the verification results for US-Ne1; (**m**–**r**) show the verification results for US-Ne2; (**s**–**x**) show the verification results for US-Ne3; (**y**–**aa**) show the verification results for Daman; (**ab**–**ad**) show the verification results for Fenzidi.

4.2. Comparison with the V_{m25} Obtained by BESS

The V_{m25} calculated by BESS, BESS_P and our Two-stage linear model were compared in simulating the time series of V_{m25} inversely solved by coupling the BESS and LRC using EC data at the five flux sites (Figure 5). Unfortunately, the flux data for Daman in 2020 and Fenzidi in 2017 are incomplete; and due to the partial lack of remote sensing and meteorological data, the V_{m25} inverted by LRC for US-Ne1 and US-Ne2 sites in 2001 is also incomplete. The BESS model consistently underestimates V_{m25} throughout the growth period due to the fixed low PeakV_{m25} value, with the discrepancy becoming particularly noticeable during the middle stages of the growth period. Conversely, towards the end of the

growth period when V_{m25} values are low, BESS tends to overestimate V_{m25}. BESS_P, which employs the same modeling approach as BESS but adjusts the PeakV_{m25} parameter, exhibiting a somewhat improved performance in estimating the trend of V_{m25} during the early growth phase. However, during the declining stage of V_{m25}, BESS_P tends to significantly overestimate the values. Due to the same formula structure, the R^2 between the calculated V_{m25} of both methods and the verified values remains consistent, ranging from 0.01 to 0.67 (Table 2). The RMSE of the BESS model ranges from 13.25 to 18.93 μmol $m^{-2}s^{-1}$ and the RMSE of the BESS_P ranges from 15.30 to 25.07 μmol $m^{-2}s^{-1}$. Despite the adjustment in PeakV_{m25}, both BESS and BESS_P demonstrate poor performance in fitting the trend in V_{m25} across all sites. The observations reveal a distinct pattern of V_{m25} initially rising before declining, and our Two-stage linear model effectively captures this seasonal variation in V_{m25}, with R^2 ranges from 0.71 to 0.88 and RMSE ranges from 5.40 to 7.54 μmol $m^{-2}s^{-1}$. During the early stages of crop growth, V_{m25} generally exhibits an upward trajectory, albeit with significant diurnal fluctuations. Conversely, in the descending phase, V_{m25} tends to display a more linear decline with reduced fluctuation.

4.3. Comparison with the GPP Obtained by BESS

To evaluate the role of the Two-stage linear model in improving GPP simulation, we compared the GPP simulation results using BESS, BESS_P and our Two-stage linear model for calculating V_{m25}, and validated them with flux site GPP data (Figure 6, Table 3). The results indicate that the original BESS model consistently underestimates GPP across all five sites. On average, GPP is underestimated by 12.60%, with the most significant underestimation observed at US-Ne2 (16.29%). Similarly, BESS_P generally overestimates GPP, averaging 20.73% across all sites, with the most significant overestimation recorded at US-Ne1 (24.05%). In contrast, the GPP simulated by BESS incorporating our Two-stage linear model exhibits a strong correlation with the flux site's observed GPP data, with RMSE ranging from 2.03 to 2.32 gC $m^{-2}d^{-1}$ and R^2 ranging from 0.82 to 0.90. On average, GPP is only underestimated by 0.85% across all sites. The most substantial underestimation occurs at Daman (16.38%), while the most significant overestimation is at Fenzidi (4.60%). The simulation result of BESS_TL significantly outperform the BESS and BESS_P in GPP estimation.

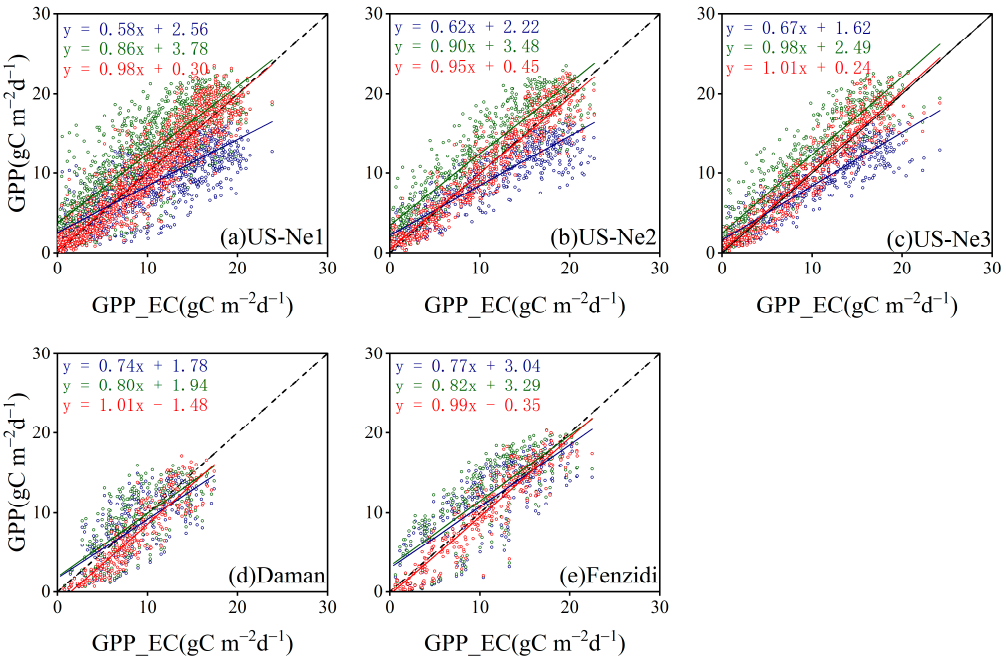

Figure 6. The GPP calculated by BESS (blue dots and trend lines), BESS_P (green dots and trend lines), and BESS_TL (red dots and trend lines) vs. flux site observed GPP (GPP_EC) at (**a**) US-Ne1, (**b**) US-Ne2, (**c**) US-Ne3, (**d**) Daman, (**e**) Fenzidi.

Table 3. The performance of the original BESS, BESS_P and BESS_TL in estimating observed GPP at the five flux sites.

Site	BESS		BESS_P		BESS_TL	
	RMSE	R^2	RMSE	R^2	RMSE	R^2
US-Ne1	3.69	0.66	4.07	0.70	2.29	0.86
US-Ne2	3.48	0.80	3.53	0.83	2.03	0.90
US-Ne3	2.99	0.83	3.32	0.85	2.04	0.89
Daman	2.96	0.53	3.02	0.53	2.32	0.82
Fenzidi	3.35	0.63	3.64	0.63	2.06	0.87

To better reveal the role of the Two-stage linear model in improving GPP simulation, the discrepancy of the annual GPP estimation by BESS, BESS_P and BESS_TL were compared (Figures 7 and 8). The mean GPP estimation discrepancy by BESS, BESS_P and BESS_TL are −1.56, 2.39 and 0.12 gC $m^{-2}d^{-1}$ in US-Ne1, respectively, with the corresponding standard deviations of 3.35, 3.30 and 2.29 gC $m^{-2}d^{-1}$ (Table 4). Except for the Daman site, the means and standard deviations of GPP discrepancy of BESS_TL estimation are closer to 0 for most years compared to the BESS and BESS_P estimation (Table 4). At the Daman site, although the absolute value of the mean GPP estimation discrepancy of BESS_TL is greater than that of BESS, the standard deviation of BESS_TL GPP estimation discrepancy remains the smallest. Thus, it can be concluded that BESS_TL effectively enhances the simulation accuracy of GPP.

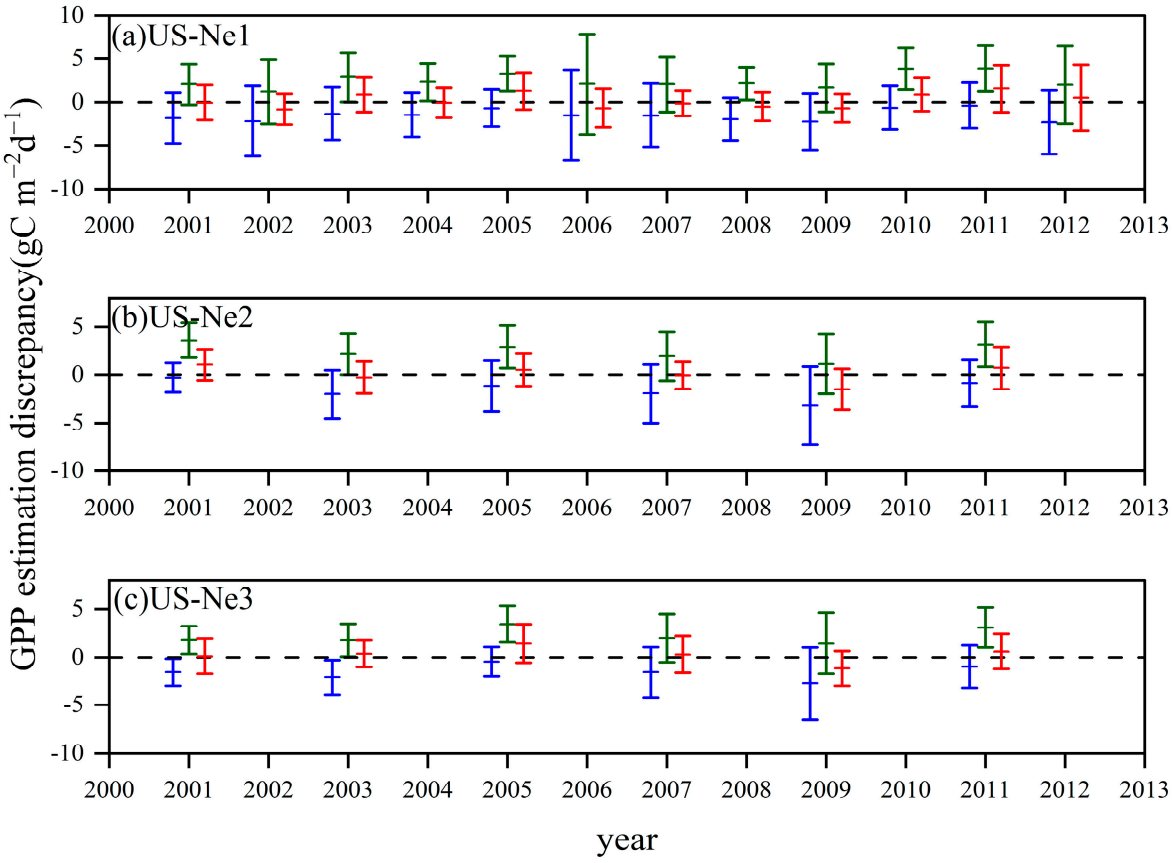

Figure 7. The annual GPP estimation discrepancy of the BESS (blue lines), BESS_P (green lines) and BESS_TL (red lines) at (**a**) US-Ne1, (**b**) US-Ne2, (**c**) US-Ne3.

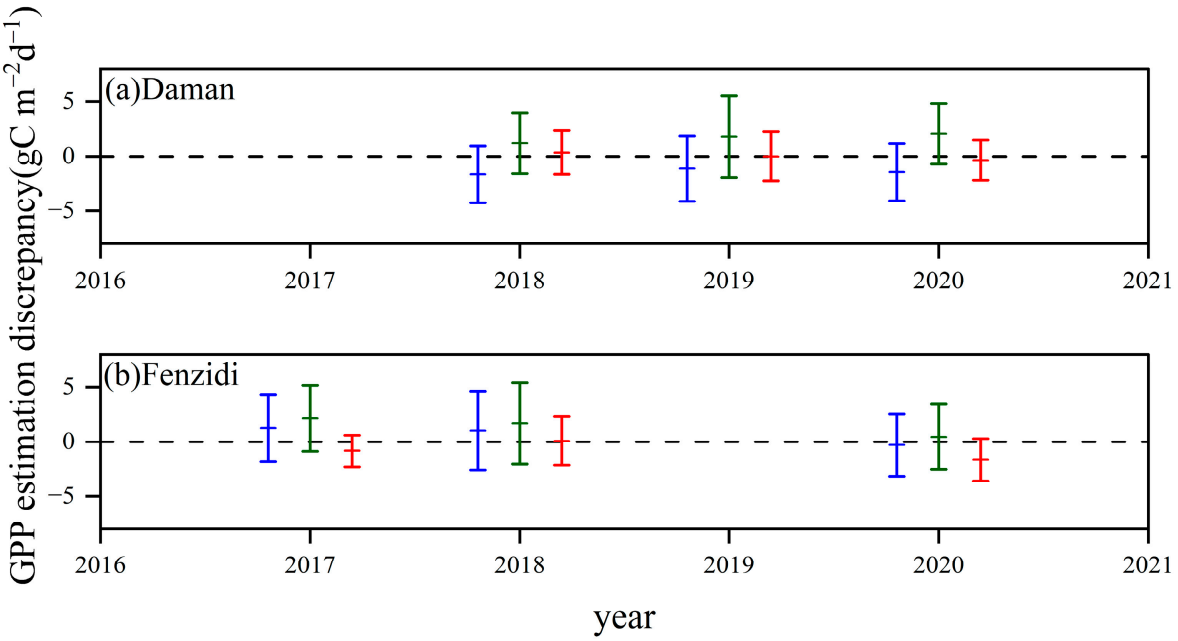

Figure 8. The annual GPP estimation discrepancy of the BESS (blue lines), BESS_P (green lines) and BESS_TL (red lines) at (**a**) Daman, (**b**) Fenzidi.

Table 4. Mean and standard deviation of the GPP results by the three methods in each site (gC m^{-2}d^{-1}).

Site	BESS		BESS_P		BESS_TL	
	Mean	Std	Mean	Std	Mean	Std
US-Ne1	−1.56	3.35	2.39	3.30	0.12	2.29
US-Ne2	−1.69	3.03	2.40	2.59	−0.02	2.03
US-Ne3	−1.56	2.56	2.31	3.32	0.29	2.02
Daman	−0.43	2.92	0.22	3.01	−1.42	1.82
Fenzidi	−0.06	3.29	−0.13	3.49	0.05	2.00

To provide a clearer view of the simulation results of the three methods, the seasonal variation in the GPP difference between the simulated GPP and EC observations is represented in Figures 9 and 10. Figure 9 displays the annual simulation results for each site, while Figure 10 presents the multi-year average simulation outcomes across all sites. Significant seasonal differences are evident in the simulation outputs of all three methods. The original BESS model tends to slightly overestimate GPP towards the end of the growth period and underestimates during other times, particularly in the mid-growth period, where the underestimation is pronounced. Conversely, BESS_P demonstrates satisfactory simulations only during the early growth period, followed by a gradual overestimation of GPP. BESS_TL outperforms the other two methods in capturing seasonal shifts in GPP. The discrepancy between the simulated GPP and EC values remains relatively close to zero. GPP is slightly underestimated during the early and late growth stages and slightly overestimated during the mid-growth stage. Overall, BESS_TL demonstrates a more balanced performance across different growth stages compared to BESS and BESS_P.

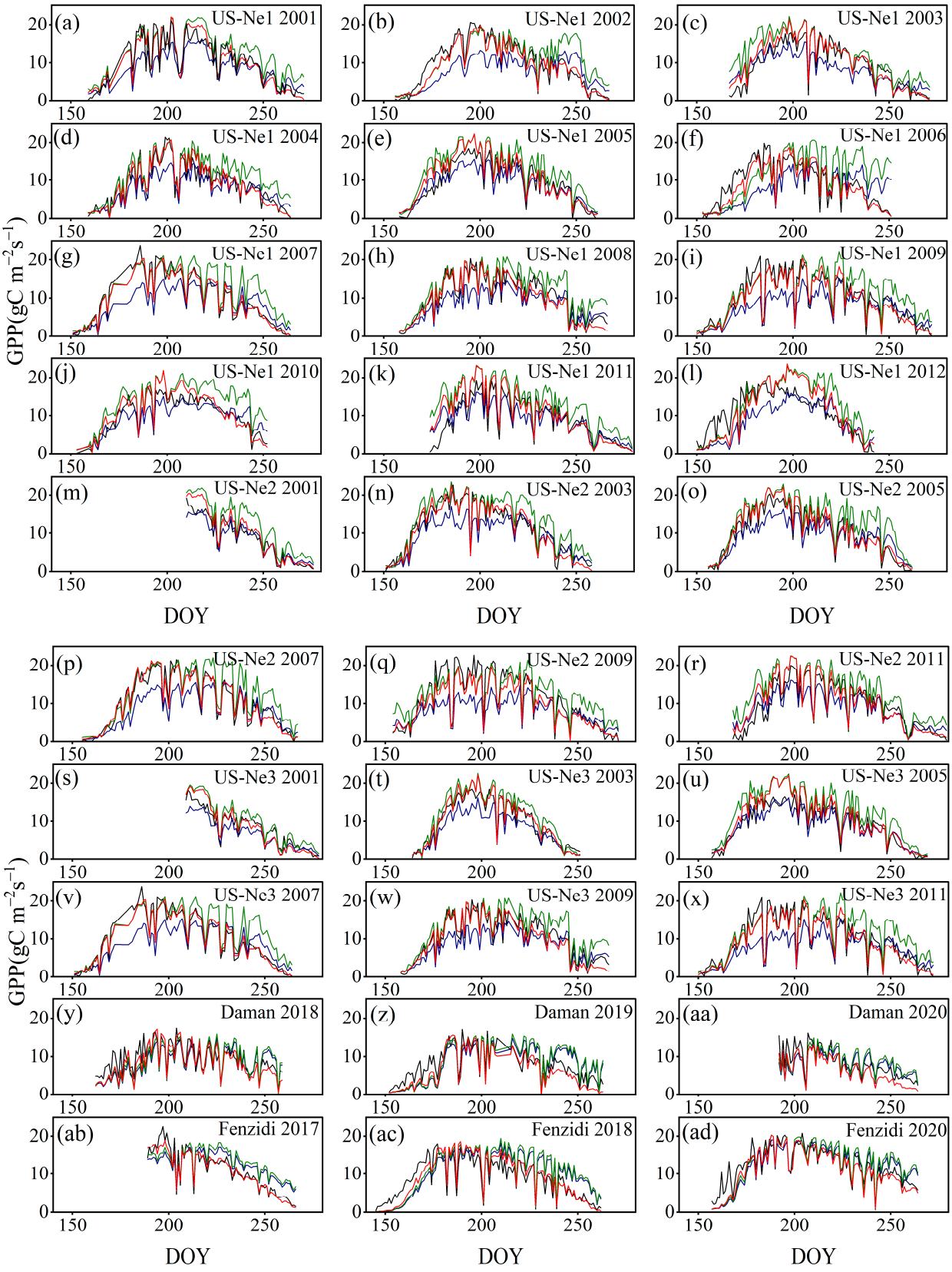

Figure 9. The estimation of daily GPP provided by BESS (blue lines), BESS_P (green lines) and BESS_TL (red lines) compared to observation by flux sites (black lines).

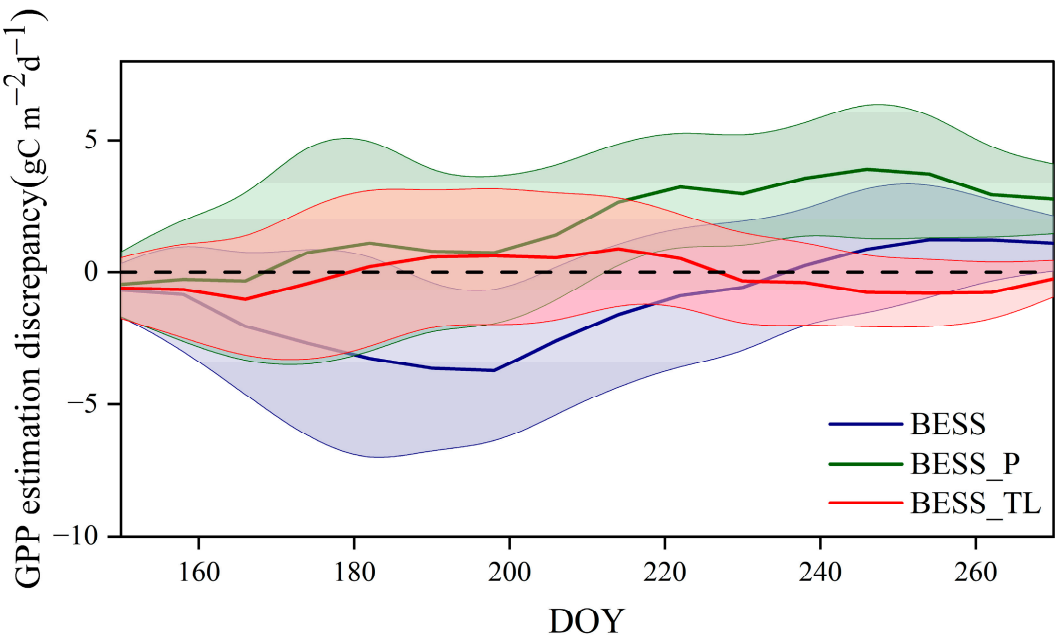

Figure 10. The daily GPP estimation discrepancy of BESS (blue lines), BESS_P (green lines) and BESS_TL (red lines). The center lines are the multi-year averages, and the edges of the shadow area are mean ± standard deviation.

5. Discussion

5.1. Foundation of V_{m25} Estimation

This study highlights the importance of considering seasonal changes in the photosynthetic capacity of crops. However, estimating the temporal changes in V_{m25} remains challenging. The method to inverting the time series of V_{m25} by coupling the BEPS model and LRC has already been proposed. However, the BEPS model does not account for C4 plants [31,32]. In our research, we addressed this challenge by inverting V_{m25} for five maize sites through the coupling of the BESS model with LRC. This approach enabled us to estimate V_{m25} without relying on extensive gas exchange experiments. To achieve this, we utilized field measurements of EC data and remote sensing data. The BESS model, which replaces the original BEPS model, incorporates specific considerations for the photosynthesis of C4 plants like maize [56]. After removing the data from periods of low radiation, V_{m25} exhibited a significant trend of initially increasing and then decreasing (Figure 5). Furthermore, V_{m25} showed a strong correlation with leaf age when the growing period was divided into two phases (Figure 2). This relationship provides the basis for our research.

5.2. The Advantages of Leaf Age as a V_{m25} Predictor

Annual plants complete their entire life cycle within one growing season. Starting from seeds, they progress through stages of germination, growth, flowering, fruiting, and ultimately die, all within a single year. In contrast, perennials continue to grow and reproduce for several years or more. Compared to perennial plants, using annual plants as research subjects eliminates the need to consider interannual influences and allows for easier identification of their developmental stages. This simplification makes it more straightforward to study the relationship between leaf age and V_{m25}.

Our Two-stage linear model takes the advantage of leaf age and effectively captures the V_{m25} seasonal variation with the crop growth processes. Maize, being annual plants, undergo significant changes in photosynthetic capacity throughout their growth cycle due to various physiological characteristics. Typically, V_{m25} exhibits only one peak value during the entire crop growth period [33]. This uniqueness of the crop is the basis for our proposed model. In our model, the basic assumption is that the photosynthetic capacity increases during leaf development, reaching a maximum in spring or early summer, stabilizing or

gradually decreasing in summer, and further decreasing during senescence [6,84]. Comparably, our model, in which V_{m25} is quantified with leaf age, can perform well due to the strong correlation between V_{m25} and leaf age (Figure 2). Now, it is understandable that the performance of the existing empirical relationships established between V_{m25} and other variables, such as N_{Leaf}, Chll, and photoperiod, is basically determined by the similarity of that variable to the leaf age [7,8,40,85]. Also, the photosynthetic capacity and environmental factors are often mismatched [57].

For the estimation of V_{m25}, our Two-stage linear model outperforms both the original BESS model and BESS_P. The main difference between the original BESS model and BESS_P is the PeakV_{m25}: PeakV_{m25} in the original BESS model is fixed, whereas the PeakV_{m25} in the BESS_P is the same as the PeakV_{m25} in our Two-stage linear model. Thus, solely improving the PeakV_{m25} cannot solve the problem. In the original BESS model and BESS_P, LAI is used to seasonalize V_{m25} [56]. However, it is proven that the correlation between V_{m25} and LAI is not as strong as leaf age in the later half stage of crop growth (Figure 2) because the leaves turn yellow and senesce with the senescence of crops, but the change in LAI is not significant. Furthermore, the BESS model coupled with the Two-stage linear model (BESS_TL) has significantly improved the simulation of GPP. Across the five maize sites, BESS_TL only underestimated GPP by an average of 0.85%. In contrast, the original BESS model underestimated GPP by an average of 12.60%, and the BESS_P model overestimated GPP by an average of 20.73%. The superior performance of our Two-stage linear model underscores the importance of considering PeakV_{m25} and leaf age in accurately modeling V_{m25}.

5.3. Readily Available Leaf Age

Leaf age, an important indicator of crop physiological characteristics, is usually relatively easy to obtain. The emergence date can be directly observed in the field, allowing for straightforward counting to determine leaf age [62]. Additionally, remote sensing technologies offer a powerful tool for estimating leaf age across large areas of farmland [86,87]. By calculating vegetation indices from remote sensing images, we can indirectly assess the growth stage of leaves. These indices exhibit specific patterns of change as the leaves progress from young to mature and eventually to senescent stages. By analyzing these patterns, we can accurately infer leaf age.

5.4. Model Limitations

Due to data availability, our Two-stage linear model was only validated with maize data from five flux sites. Its applicability to other sites relies on the quality of their own flux data. Also, our Two-stage linear model is derived from maize sites, and its applicability to other vegetation types requires further validation. While other vegetation types have also demonstrated a close correlation between V_{m25} and leaf age [8,58,63,64], extending this method to other vegetation types, such as perennial plants, presents additional challenges. Perennials often have canopies that consist of leaves at various stages of development, ranging from young and fully functional to older and senescent leaves [63]. This variation necessitates a more nuanced approach to modeling V_{m25} in perennials, one that can account for the complex age structure of their canopies [58].

6. Conclusions

As numerous studies have highlighted, V_{m25} is a crucial parameter for calculating the photosynthesis rate. The accurate estimation of V_{m25} is essential for the regional and global modeling of ecological systems. Although various indicators have been developed to characterize V_{m25}, accurately quantifying its dynamic changes remains challenging.

(1) V_{m25} inversion: Considering the special photosynthetic process of C4 plants, we replaced the BEPS model with the BESS model coupled with the LRC to invert V_{m25} at five maize sites. This method allowed us to obtain continuous V_{m25} values throughout the growth period, enabling a detailed study of V_{m25} variation trends.

(2) Two-Stage Linear Model Development: We developed a new Two-stage linear model to determine the dynamics changes in maize V_{m25}. This method divides V_{m25} into two stages during the growth process and uses leaf age as the key variable in the simulation, effectively capturing the seasonal variation characteristics of V_{m25}. Additionally, compared to using a fixed value, this method allows for the calibration of the PeakV_{m25} value, thereby enhancing model accuracy.

(3) Model Performance and Comparison: The Two-stage linear method more accurately simulated the variation trend of V_{m25} compared to the V_{m25} of the original BESS model. Furthermore, implementing this method significantly improved the simulation results of GPP. BESS_TL outperforms the other two methods in this study, showing higher R^2 and lower RMSE at each site. The GPP simulated by BESS_TL at both interannual and seasonal levels deviated less from the EC GPP. Overall, the developed V_{m25} estimation method enhances the accuracy of farmland GPP simulation.

Author Contributions: Conceptualization, X.Z. and Z.H.; methodology, X.Z. and S.W.; validation, X.Z. and S.W.; data curation, W.W. and Y.R.; writing—original draft preparation, X.Z.; writing—review and editing, C.W. and Z.H.; supervision, C.Z.; project administration, C.Z. and Z.H.; funding acquisition, Z.H. All authors have read and agreed to the published version of the manuscript.

Funding: This research was funded by the National Natural Science Foundation of China (Grant Numbers: 52130902 and 52279050), and the National Key Research and Development Program of China (Grant Number: 2021YFD1900603). Research project of Inner Mongolia (NMKJXM202208).

Data Availability Statement: The original contributions presented in the study are included in the article further inquiries can be directed to the corresponding author.

Acknowledgments: We are grateful to the data providers at US-Ne1, US-Ne2, US-Ne3, and Daman sites. The dataset of Daman is provided by National Tibetan Plateau Data Center (http://data.tpdc.ac.cn (accessed on 1 March 2023)). The dataset of US-Ne1, US-Ne2 and US-Ne3 is provided by FLUXNET2015 (FLUXNET). The authors would like to thank the Editor and all reviewers whose insightful suggestions have significantly improved this paper.

Conflicts of Interest: The authors declare no conflicts of interest.

Appendix A. Result of Machine Learning Simulation of LAI

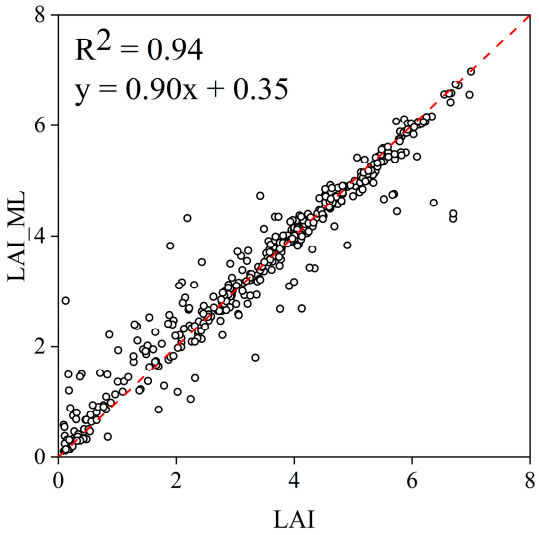

Figure A1. Machine learning training result for LAI using ExtraTreesRegressor.

Appendix B. Two-Leaf Canopy Radiative Transfer Model in BESS

A two-leaf canopy radiative transfer model is used to calculate PAR absorbed by sunlit leaves and shade leaves [56]. This method modified the PAR penetration model [88] by incorporating foliar clumping and reflected PAR from the soil.

The total absorbed incoming PAR by the canopy is

$$Q_{P\downarrow} = (1-\rho_{cbP})I_{Pb}(0)\left[1-\exp\left(-k'_{Pb}L_c\Omega\right)\right] + (1-\rho_{cdP})I_{Pd}(0)\left[1-\exp\left(-k'_{Pd}L_c\Omega\right)\right] \quad (A1)$$

where $I_{Pb}(0)$ and $I_{Pd}(0)$ are direct beam and diffuse PAR at the top of the canopy, respectively. L_c indicates the leaf area index. ρ_{cbP} and ρ_{cdP} are canopy reflectance for beam and diffuse PAR, respectively. k'_{Pb} and k'_{Pd} are the extinction coefficient for beam and scattered beam PAR, and for diffuse and scattered diffuse PAR, respectively.

The absorbed incoming beam PAR by sunlit leaves is

$$Q_{PbSun\downarrow} = I_{Pb}(0)(1-\sigma_{PAR})[1-\exp(-k_bL_c\Omega)] \quad (A2)$$

where σ_{PAR} is the leaf scattering coefficient for PAR. k_b is the extinction coefficient for black leaves.

The absorbed incoming diffuse PAR by sunlit leaves is

$$Q_{PdSun\downarrow} = \frac{I_{Pd}(0)(1-\rho_{cdP})\left[1-\exp\left(-\left(k'_{Pd}+k_b\right)L_c\Omega\right)\right]k'_{Pd}}{\left(k'_{Pd}+k_b\right)} \quad (A3)$$

The absorbed incoming scattered PAR by sunlit leaves is

$$Q_{PsSun\downarrow} = I_{Pb}(0)\left[\begin{array}{c}\frac{(1-\rho_{cbP})\left(1-\exp\left(-\left(k'_{Pb}+k_b\right)L_c\Omega\right)\right)k'_{Pb}}{\left(k'_{Pb}+k_b\right)} \\ -\frac{(1-\sigma_{PAR})(1-\exp(-2k_bL_c\Omega))}{2}\end{array}\right] \quad (A4)$$

The total absorbed incoming PAR by sunlit leaves is

$$Q_{PSun\downarrow} = Q_{PbSun\downarrow} + Q_{PdSun\downarrow} + Q_{PsSun\downarrow} \quad (A5)$$

The total absorbed incoming PAR by shade leaves is

$$Q_{PSh\downarrow} = Q_{P\downarrow} - Q_{PSun\downarrow} \quad (A6)$$

A portion of the incoming PAR passes through the canopy to the soil surface and is reflected upward into the canopy, which may be important in an open canopy with bright background. The PAR absorbed by sunlit leaves due to soil reflection is

$$\begin{array}{c}Q_{PSun\uparrow} = \left[(1-\rho_{cbP})I_{Pb}(0) + (1-\rho_{cdP})I_{Pd}(0) - \left(Q_{PSun\downarrow} + Q_{PSh\downarrow}\right)\right] \\ \times\rho_{sP}\times\exp\left(-k'_{Pd}L_c\Omega\right)\end{array} \quad (A7)$$

where ρ_{sP} is the soil reflectance for PAR.

The PAR absorbed by shade leaves due to soil reflection is

$$\begin{array}{c}Q_{PSh\uparrow} = \left[(1-\rho_{cbP})I_{Pb}(0) + (1-\rho_{cdP})I_{Pd}(0) - \left(Q_{PSun\downarrow} + Q_{PSh\downarrow}\right)\right] \\ \times\rho_{sP}\times\left[1-\exp\left(-k'_{Pd}L_c\Omega\right)\right]\end{array} \quad (A8)$$

The total PAR absorbed by sunlit and shade leaves is

$$APAR_{Sun} = Q_{PSun\downarrow} + Q_{PSun\uparrow} \quad (A9)$$

$$APAR_{Sh} = Q_{PSh\downarrow} + Q_{PSh\uparrow} \quad (A10)$$

References

1. Beer, C.; Reichstein, M.; Tomelleri, E.; Ciais, P.; Jung, M.; Carvalhais, N.; Rodenbeck, C.; Arain, M.A.; Baldocchi, D.; Bonan, G.B.; et al. Terrestrial gross carbon dioxide uptake: Global distribution and covariation with climate. *Science* **2010**, *329*, 834–838. [CrossRef] [PubMed]
2. Li, X.L.; Liang, S.L.; Yu, G.R.; Yuan, W.P.; Cheng, X.; Xia, J.Z.; Zhao, T.B.; Feng, J.M.; Ma, Z.G.; Ma, M.G.; et al. Estimation of gross primary production over the terrestrial ecosystems in China. *Ecol. Model.* **2013**, *261*, 80–92. [CrossRef]
3. Yuan, W.P.; Liu, S.G.; Yu, G.R.; Bonnefond, J.M.; Chen, J.Q.; Davis, K.; Desai, A.R.; Goldstein, A.H.; Gianelle, D.; Rossi, F.; et al. Global estimates of evapotranspiration and gross primary production based on MODIS and global meteorology data. *Remote Sens. Environ.* **2010**, *114*, 1416–1431. [CrossRef]
4. Smith, N.G.; Keenan, T.F.; Colin Prentice, I.; Wang, H.; Wright, I.J.; Niinemets, Ü.; Crous, K.Y.; Domingues, T.F.; Guerrieri, R.; Ishida, F.Y.; et al. Global photosynthetic capacity is optimized to the environment. *Ecol. Lett.* **2019**, *22*, 506–517. [CrossRef] [PubMed]
5. Zhu, X.J.; Yu, G.R.; Wang, Q.F.; Gao, Y.N.; He, H.L.; Zheng, H.; Chen, Z.; Shi, P.L.; Zhao, L.; Li, Y.N.; et al. Approaches of climate factors affecting the spatial variation of annual gross primary productivity among terrestrial ecosystems in China. *Ecol. Indic.* **2016**, *62*, 174–181. [CrossRef]
6. Miner, G.L.; Bauerle, W.L. Seasonal responses of photosynthetic parameters in maize and sunflower and their relationship with leaf functional traits. *Plant Cell Environ.* **2019**, *42*, 1561–1574. [CrossRef]
7. Rogers, A.; Medlyn, B.E.; Dukes, J.S.; Bonan, G.; von Caemmerer, S.; Dietze, M.C.; Kattge, J.; Leakey, A.D.; Mercado, L.M.; Niinemets, U.; et al. A roadmap for improving the representation of photosynthesis in Earth system models. *New Phytol.* **2017**, *213*, 22–42. [CrossRef] [PubMed]
8. Wang, S.Q.; Li, Y.; Ju, W.M.; Chen, B.; Chen, J.H.; Croft, H.; Mickler, R.A.; Yang, F.T. Estimation of Leaf Photosynthetic Capacity From Leaf Chlorophyll Content and Leaf Age in a Subtropical Evergreen Coniferous Plantation. *J. Geophys. Res. Biogeosci.* **2020**, *125*, e2019JG005020. [CrossRef]
9. Zhang, Y.Q.; Kong, D.D.; Gan, R.; Chiew, F.H.S.; McVicar, T.R.; Zhang, Q.; Yang, Y.T. Coupled estimation of 500 m and 8-day resolution global evapotranspiration and gross primary production in 2002-2017. *Remote Sens. Environ.* **2019**, *222*, 165–182. [CrossRef]
10. Liu, J.; Chen, J.M.; Cihlar, J. Mapping evapotranspiration based on remote sensing: An application to Canada's landmass. *Water Resources Res.* **2003**, *39*, 1189. [CrossRef]
11. Farquhar, G.D.; Caemmerer, S.V.; Berry, J.A. A biochemical model of photosynthetic assimilation in leaves of C3 species. *Planta* **1980**, *149*, 67–90. [CrossRef]
12. Collatz, G.J.; Ribas-Carbo, M.; Berry, J.A. Coupled Photosynthesis-Stomatal Conductance Model for Leaves of C4 Plants. *Aust. J. Plant Physiol.* **1992**, *19*, 519–538. [CrossRef]
13. Lebauer, D.S.; Wang, D.; Richter, K.T.; Davidson, C.C.; Dietze, M.C. Facilitating feedbacks between field measurements and ecosystem models. *Ecol. Monogr.* **2013**, *83*, 133–154. [CrossRef]
14. Bonan, G.B.; Lawrence, P.J.; Oleson, K.W.; Levis, S.; Jung, M.; Reichstein, M.; Lawrence, D.M.; Swenson, S.C. Improving canopy processes in the Community Land Model version 4 (CLM4) using global flux fields empirically inferred from FLUXNET data. *J. Geophys. Res. Biogeosci.* **2011**, *116*, G02014. [CrossRef]
15. Medvigy, D.; Jeong, S.J.; Clark, K.L.; Skowronski, N.S.; Schafer, K.V.R. Effects of seasonal variation of photosynthetic capacity on the carbon fluxes of a temperate deciduous forest. *J. Geophys. Res. Biogeosci.* **2013**, *118*, 1703–1714. [CrossRef]
16. Grassi, G.; Vicinelli, E.; Ponti, F.; Cantoni, L.; Magnani, F. Seasonal and interannual variability of photosynthetic capacity in relation to leaf nitrogen in a deciduous forest plantation in northern Italy. *Tree Physiol.* **2005**, *25*, 349–360. [CrossRef] [PubMed]
17. Yuan, D.K.; Zhang, S.; Li, H.J.; Zhang, J.H.; Yang, S.S.; Bai, Y. Improving the Gross Primary Productivity Estimate by Simulating the Maximum Carboxylation Rate of the Crop Using Machine Learning Algorithms. *IEEE Trans. Geosci. Remote Sens.* **2022**, *60*, 4413115. [CrossRef]
18. Qian, X.J.; Liu, L.Y.; Chen, X.D.; Zarco-Tejada, P. Assessment of Satellite Chlorophyll-Based Leaf Maximum Carboxylation Rate (Vcmax) Using Flux Observations at Crop and Grass Sites. *IEEE J. Sel. Top. Appl. Earth Obs. Remote Sens.* **2021**, *14*, 5352–5360. [CrossRef]
19. Houborg, R.; Cescatti, A.; Migliavacca, M.; Kustas, W.P. Satellite retrievals of leaf chlorophyll and photosynthetic capacity for improved modeling of GPP. *Agric. For. Meteorol.* **2013**, *177*, 10–23. [CrossRef]
20. Zhang, Y.; Guanter, L.; Berry, J.A.; Joiner, J.; van der Tol, C.; Huete, A.; Gitelson, A.; Voigt, M.; Kohler, P. Estimation of vegetation photosynthetic capacity from space-based measurements of chlorophyll fluorescence for terrestrial biosphere models. *Glob. Chang. Biol.* **2014**, *20*, 3727–3742. [CrossRef]
21. Chen, J.M.; Mo, G.; Pisek, J.; Liu, J.; Deng, F.; Ishizawa, M.; Chan, D. Effects of foliage clumping on the estimation of global terrestrial gross primary productivity. *Glob. Biogeochem. Cycles* **2012**, *26*, GB1019. [CrossRef]
22. Gan, R.; Zhang, Y.Q.; Shi, H.; Yang, Y.T.; Eamus, D.; Cheng, L.; Chiew, F.H.S.; Yu, Q. Use of satellite leaf area index estimating evapotranspiration and gross assimilation for Australian ecosystems. *Ecohydrology* **2018**, *11*, e1974. [CrossRef]
23. Dillen, S.Y.; Op de Beeck, M.; Hufkens, K.; Buonanduci, M.; Phillips, N.G. Seasonal patterns of foliar reflectance in relation to photosynthetic capacity and color index in two co-occurring tree species, Quercus rubra and Betula papyrifera. *Agric. For. Meteorol.* **2012**, *160*, 60–68. [CrossRef]

24. Croft, H.; Chen, J.M.; Luo, X.; Bartlett, P.; Chen, B.; Staebler, R.M. Leaf chlorophyll content as a proxy for leaf photosynthetic capacity. *Glob. Chang. Biol.* **2017**, *23*, 3513–3524. [CrossRef] [PubMed]
25. Jiang, C.; Ryu, Y.; Wang, H.; Keenan, T.F. An optimality-based model explains seasonal variation in C3 plant photosynthetic capacity. *Glob. Chang. Biol.* **2020**, *26*, 6493–6510. [CrossRef] [PubMed]
26. Bloomfield, K.J.; Prentice, I.C.; Cernusak, L.A.; Eamus, D.; Medlyn, B.E.; Rumman, R.; Wright, I.J.; Boer, M.M.; Cale, P.; Cleverly, J.; et al. The validity of optimal leaf traits modelled on environmental conditions. *New Phytol.* **2019**, *221*, 1409–1423. [CrossRef] [PubMed]
27. Wang, H.; Atkin, O.K.; Keenan, T.F.; Smith, N.G.; Wright, I.J.; Bloomfield, K.J.; Kattge, J.; Reich, P.B.; Prentice, I.C. Acclimation of leaf respiration consistent with optimal photosynthetic capacity. *Glob. Chang. Biol.* **2020**, *26*, 2573–2583. [CrossRef] [PubMed]
28. Chen, B.; Wang, P.Y.; Wang, S.Q.; Ju, W.M.; Liu, Z.H.; Zhang, Y.H. Simulating canopy carbonyl sulfide uptake of two forest stands through an improved ecosystem model and parameter optimization using an ensemble Kalman filter. *Ecol. Model.* **2023**, *475*, 110212. [CrossRef]
29. Mo, X.G.; Chen, J.M.; Ju, W.M.; Black, T.A. Optimization of ecosystem model parameters through assimilating eddy covariance flux data with an ensemble Kalman filter. *Ecol. Model.* **2008**, *217*, 157–173. [CrossRef]
30. Xu, T.R.; Chen, F.; He, X.L.; Barlage, M.; Zhang, Z.; Liu, S.M.; He, X.P. Improve the Performance of the Noah-MP-Crop Model by Jointly Assimilating Soil Moisture and Vegetation Phenology Data. *J. Adv. Model. Earth Syst.* **2021**, *13*, e2020MS002394. [CrossRef]
31. Zheng, T.; Chen, J.; He, L.M.; Arain, M.A.; Thomas, S.C.; Murphy, J.G.; Geddes, J.A.; Black, T.A. Inverting the maximum carboxylation rate (V-cmax) from the sunlit leaf photosynthesis rate derived from measured light response curves at tower flux sites. *Agric. For. Meteorol.* **2017**, *236*, 48–66. [CrossRef]
32. Xie, X.Y.; Li, A.N.; Jin, H.A.; Yin, G.F.; Nan, X. Derivation of temporally continuous leaf maximum carboxylation rate (V-cmax) from the sunlit leaf gross photosynthesis productivity through combining BEPS model with light response curve at tower flux sites. *Agric. For. Meteorol.* **2018**, *259*, 82–94. [CrossRef]
33. Wang, X.P.; Chen, J.M.; Ju, W.M.; Zhang, Y.G. Seasonal Variations in Leaf Maximum Photosynthetic Capacity and Its Dependence on Climate Factors Across Global FLUXNET Sites. *J. Geophys. Res. Biogeosci.* **2022**, *127*, e2021JG006709. [CrossRef]
34. Gamon, J.A.; Field, C.B.; Goulden, M.L.; Griffin, K.L.; Hartley, A.E.; Joel, G.; Penuelas, J.; Valentini, R. Relationships between Ndvi, Canopy Structure, and Photosynthesis in 3 Californian Vegetation Types. *Ecol. Appl.* **1995**, *5*, 28–41. [CrossRef]
35. Alton, P.B. Retrieval of seasonal Rubisco-limited photosynthetic capacity at global FLUXNET sites from hyperspectral satellite remote sensing: Impact on carbon modelling. *Agric. For. Meteorol.* **2017**, *232*, 74–88. [CrossRef]
36. Ryu, Y.; Berry, J.A.; Baldocchi, D.D. What is global photosynthesis? History, uncertainties and opportunities. *Remote Sens. Environ.* **2019**, *223*, 95–114. [CrossRef]
37. Jin, J.; Pratama, B.A.; Wang, Q. Tracing Leaf Photosynthetic Parameters Using Hyperspectral Indices in an Alpine Deciduous Forest. *Remote Sens.* **2020**, *12*, 1124. [CrossRef]
38. Serbin, S.P.; Singh, A.; Desai, A.R.; Dubois, S.G.; Jablonsld, A.D.; Kingdon, C.C.; Kruger, E.L.; Townsend, P.A. Remotely estimating photosynthetic capacity, and its response to temperature, in vegetation canopies using imaging spectroscopy. *Remote Sens. Environ.* **2015**, *167*, 78–87. [CrossRef]
39. Kattge, J.; Knorr, W.; Raddatz, T.; Wirth, C. Quantifying photosynthetic capacity and its relationship to leaf nitrogen content for global-scale terrestrial biosphere models. *Glob. Chang. Biol.* **2009**, *15*, 976–991. [CrossRef]
40. Archontoulis, S.V.; Yin, X.; Vos, J.; Danalatos, N.G.; Struik, P.C. Leaf photosynthesis and respiration of three bioenergy crops in relation to temperature and leaf nitrogen: How conserved are biochemical model parameters among crop species? *J. Exp. Bot.* **2012**, *63*, 895–911. [CrossRef]
41. Yamori, W.; Nagai, T.; Makino, A. The rate-limiting step for CO_2 assimilation at different temperatures is influenced by the leaf nitrogen content in several C3 crop species. *Plant Cell Environ.* **2011**, *34*, 764–777. [CrossRef] [PubMed]
42. Zhang, Y.G.; Guanter, L.; Joiner, J.; Song, L.; Guan, K.Y. Spatially-explicit monitoring of crop photosynthetic capacity through the use of space-based chlorophyll fluorescence data. *Remote Sens. Environ.* **2018**, *210*, 362–374. [CrossRef]
43. Luo, X.; Croft, H.; Chen, J.M.; He, L.; Keenan, T.F. Improved estimates of global terrestrial photosynthesis using information on leaf chlorophyll content. *Glob. Chang. Biol.* **2019**, *25*, 2499–2514. [CrossRef] [PubMed]
44. Houborg, R.; McCabe, M.F.; Cescatti, A.; Gitelson, A.A. Leaf chlorophyll constraint on model simulated gross primary productivity in agricultural systems. *Int. J. Appl. Earth Obs. Geoinf.* **2015**, *43*, 160–176. [CrossRef]
45. Qian, X.; Liu, L.; Croft, H.; Chen, J. Relationship Between Leaf Maximum Carboxylation Rate and Chlorophyll Content Preserved Across 13 Species. *J. Geophys. Res. Biogeosci.* **2021**, *126*, e2020JG006076. [CrossRef]
46. Qian, B.X.; Ye, H.C.; Huang, W.J.; Xie, Q.Y.; Pan, Y.H.; Xing, N.C.; Ren, Y.; Guo, A.T.; Jiao, Q.J.; Lan, Y.B. A sentinel-2-based triangular vegetation index for chlorophyll content estimation. *Agric. For. Meteorol.* **2022**, *322*, 109000. [CrossRef]
47. Genty, B.; Briantais, J.M.; Baker, N.R. The Relationship between the Quantum Yield of Photosynthetic Electron-Transport and Quenching of Chlorophyll Fluorescence. *Biochim. Et Biophys. Acta (BBA)-Gen. Subj.* **1989**, *990*, 87–92. [CrossRef]
48. Yang, X.; Tang, J.W.; Mustard, J.F.; Lee, J.E.; Rossini, M.; Joiner, J.; Munger, J.W.; Kornfeld, A.; Richardson, A.D. Solar-induced chlorophyll fluorescence that correlates with canopy photosynthesis on diurnal and seasonal scales in a temperate deciduous forest. *Geophys. Res. Lett.* **2015**, *42*, 2977–2987. [CrossRef]

49. He, L.; Chen, J.M.; Liu, J.; Zheng, T.; Wang, R.; Joiner, J.; Chou, S.; Chen, B.; Liu, Y.; Liu, R.; et al. Diverse photosynthetic capacity of global ecosystems mapped by satellite chlorophyll fluorescence measurements. *Remote Sens. Environ.* **2019**, *232*, 111344. [CrossRef]
50. Camino, C.; Gonzalez-Dugo, V.; Hernandez, P.; Zarco-Tejada, P.J. Radiative transfer Vcmax estimation from hyperspectral imagery and SIF retrievals to assess photosynthetic performance in rainfed and irrigated plant phenotyping trials. *Remote Sens. Environ.* **2019**, *231*, 111186. [CrossRef]
51. Chen, R.A.; Liu, L.Y.; Liu, X.J. Leaf chlorophyll contents dominates the seasonal dynamics of SIF/GPP ratio: Evidence from continuous measurements in a maize field. *Agric. For. Meteorol.* **2022**, *323*, 109070. [CrossRef]
52. Jin, P.B.; Wang, Q.; Iio, A.; Tenhunen, J. Retrieval of seasonal variation in photosynthetic capacity from multi-source vegetation indices. *Ecol. Inform.* **2012**, *7*, 7–18. [CrossRef]
53. Zhou, Y.L.; Ju, W.M.; Sun, X.M.; Hu, Z.M.; Han, S.J.; Black, T.A.; Jassal, R.S.; Wu, X.C. Close relationship between spectral vegetation indices and V-cmax in deciduous and mixed forests. *Tellus B Chem. Phys. Meteorol.* **2014**, *66*, 23279. [CrossRef]
54. Muraoka, H.; Noda, H.M.; Nagai, S.; Motohka, T.; Saitoh, T.M.; Nasahara, K.N.; Saigusa, N. Spectral vegetation indices as the indicator of canopy photosynthetic productivity in a deciduous broadleaf forest. *J. Plant Ecol.* **2013**, *6*, 393–407. [CrossRef]
55. Wang, R.; Chen, J.M.; Luo, X.Z.; Black, A.; Arain, A. Seasonality of leaf area index and photosynthetic capacity for better estimation of carbon and water fluxes in evergreen conifer forests. *Agric. For. Meteorol.* **2019**, *279*, 107708. [CrossRef]
56. Ryu, Y.; Baldocchi, D.D.; Kobayashi, H.; van Ingen, C.; Li, J.; Black, T.A.; Beringer, J.; van Gorsel, E.; Knohl, A.; Law, B.E.; et al. Integration of MODIS land and atmosphere products with a coupled-process model to estimate gross primary productivity and evapotranspiration from 1 km to global scales. *Glob. Biogeochem. Cycles* **2011**, *25*, GB4017. [CrossRef]
57. Zhao, Q.; Zhu, Z.; Zeng, H.; Myneni, R.B.; Zhang, Y.; Penuelas, J.; Piao, S. Seasonal peak photosynthesis is hindered by late canopy development in northern ecosystems. *Nat. Plants* **2022**, *8*, 1484–1492. [CrossRef] [PubMed]
58. Zhou, H.; Xu, M.; Pan, H.; Yu, X. Leaf-age effects on temperature responses of photosynthesis and respiration of an alpine oak, Quercus aquifolioides, in southwestern China. *Tree Physiol.* **2015**, *35*, 1236–1248. [CrossRef] [PubMed]
59. Locke, A.M.; Ort, D.R. Leaf hydraulic conductance declines in coordination with photosynthesis, transpiration and leaf water status as soybean leaves age regardless of soil moisture. *J. Exp. Bot.* **2014**, *65*, 6617–6627. [CrossRef]
60. Reich, P.B.; Walters, M.B.; Ellsworth, D.S. Leaf Age and Season Influence the Relationships between Leaf Nitrogen, Leaf Mass Per Area and Photosynthesis in Maple and Oak Trees. *Plant Cell Environ.* **1991**, *14*, 251–259. [CrossRef]
61. Richardson, A.D.; Anderson, R.S.; Arain, M.A.; Barr, A.G.; Bohrer, G.; Chen, G.S.; Chen, J.M.; Ciais, P.; Davis, K.J.; Desai, A.R.; et al. Terrestrial biosphere models need better representation of vegetation phenology: Results from the North American Carbon Program Site Synthesis. *Glob. Chang. Biol.* **2012**, *18*, 566–584. [CrossRef]
62. Nguy-Robertson, A.; Suyker, A.; Xiao, X.M. Modeling gross primary production of maize and soybean croplands using light quality, temperature, water stress, and phenology. *Agric. For. Meteorol.* **2015**, *213*, 160–172. [CrossRef]
63. Wu, Q.L.; Song, C.H.; Song, J.L.; Wang, J.D.; Chen, S.Y.; Yang, L.; Xiang, W.H.; Zhao, Z.H.; Jiang, J. Effects of leaf age and canopy structure on gross ecosystem production in a subtropical evergreen Chinese fir forest. *Agric. For. Meteorol.* **2021**, *310*, 108618. [CrossRef]
64. Meijide, A.; Roll, A.; Fan, Y.C.; Herbst, M.; Niu, F.R.; Tiedemann, F.; June, T.; Rauf, A.; Holoscher, D.; Knohl, A. Controls of water and energy fluxes in oil palm plantations: Environmental variables and oil palm age. *Agric. For. Meteorol.* **2017**, *239*, 71–85. [CrossRef]
65. Li, S.; Fleisher, D.H.; Wang, Z.; Barnaby, J.; Timlin, D.; Reddy, V.R. Application of a coupled model of photosynthesis, stomatal conductance and transpiration for rice leaves and canopy. *Comput. Electron. Agric.* **2021**, *182*, 106047. [CrossRef]
66. Wu, J.; Albert, L.P.; Lopes, A.P.; Restrepo-Coupe, N.; Hayek, M.; Wiedemann, K.T.; Guan, K.; Stark, S.C.; Christoffersen, B.; Prohaska, N.; et al. Leaf development and demography explain photosynthetic seasonality in Amazon evergreen forests. *Science* **2016**, *351*, 972–976. [CrossRef] [PubMed]
67. Kositsup, B.; Kasemsap, P.; Thanisawanyangkura, S.; Chairungsee, N.; Satakhun, D.; Teerawatanasuk, K.; Ameglio, T.; Thaler, P. Effect of leaf age and position on light-saturated CO_2 assimilation rate, photosynthetic capacity, and stomatal conductance in rubber trees. *Photosynthetica* **2010**, *48*, 67–78. [CrossRef]
68. Lu, X.H.; Ju, W.M.; Li, J.; Croft, H.; Chen, J.M.; Luo, Y.Q.; Yu, H.; Hu, H.J. Maximum Carboxylation Rate Estimation With Chlorophyll Content as a Proxy of Rubisco Content. *J. Geophys. Res. Biogeosci.* **2020**, *125*, e2020JG005748. [CrossRef]
69. Pastorello, G.; Trotta, C.; Canfora, E.; Chu, H.S.; Christianson, D.; Cheah, Y.W.; Poindexter, C.; Chen, J.Q.; Elbashandy, A.; Humphrey, M.; et al. The FLUXNET2015 dataset and the ONEFlux processing pipeline for eddy covariance data. *Sci. Data* **2020**, *7*, 225. [CrossRef]
70. Liu, S.M.; Xu, Z.W.; Wang, W.Z.; Jia, Z.Z.; Zhu, M.J.; Bai, J.; Wang, J.M. A comparison of eddy-covariance and large aperture scintillometer measurements with respect to the energy balance closure problem. *Hydrol. Earth Syst. Sci.* **2011**, *15*, 1291–1306. [CrossRef]
71. Liu, S.M.; Li, X.; Xu, Z.W.; Che, T.; Xiao, Q.; Ma, M.G.; Liu, Q.H.; Jin, R.; Guo, J.W.; Wang, L.X.; et al. The Heihe Integrated Observatory Network: A Basin-Scale Land Surface Processes Observatory in China. *Vadose Zone J.* **2018**, *17*, 180072. [CrossRef]
72. Suyker, A.E.; Verma, S.B. Gross primary production and ecosystem respiration of irrigated and rainfed maize-soybean cropping systems over 8 years. *Agric. For. Meteorol.* **2012**, *165*, 12–24. [CrossRef]

73. Bai, Y.; Zhang, J.H.; Zhang, S.; Yao, F.M.; Magliulo, V. A remote sensing-based two-leaf canopy conductance model: Global optimization and applications in modeling gross primary productivity and evapotranspiration of crops. *Remote Sens. Environ.* **2018**, *215*, 411–437. [CrossRef]
74. Chen, J.M.; Menges, C.H.; Leblanc, S.G. Global mapping of foliage clumping index using multi-angular satellite data. *Remote Sens. Environ.* **2005**, *97*, 447–457. [CrossRef]
75. Chen, J.M.; Black, T.A. Foliage area and architecture of plant canopies from sunfleck size distributions. *Agric. For. Meteorol.* **1992**, *60*, 249–266. [CrossRef]
76. He, L.M.; Chen, J.M.; Pisek, J.; Schaaf, C.; Strahler, A.H.; IEEE. Global clumping index map derived from modis BRDF products. In Proceedings of the 2011 IEEE International Geoscience and Remote Sensing Symposium, Vancouver, BC, Canada, 24–29 July 2011; pp. 1255–1258. [CrossRef]
77. He, L.M.; Chen, J.M.; Pisek, J.; Schaaf, C.B.; Strahler, A.H. Global clumping index map derived from the MODIS BRDF product. *Remote Sens. Environ.* **2012**, *119*, 118–130. [CrossRef]
78. Lasslop, G.; Reichstein, M.; Papale, D.; Richardson, A.D.; Arneth, A.; Barr, A.; Stoy, P.; Wohlfahrt, G. Separation of net ecosystem exchange into assimilation and respiration using a light response curve approach: Critical issues and global evaluation. *Glob. Chang. Biol.* **2010**, *16*, 187–208. [CrossRef]
79. Chen, J.M.; Liu, J.; Cihlar, J.; Goulden, M.L. Daily canopy photosynthesis model through temporal and spatial scaling for remote sensing applications. *Ecol. Model.* **1999**, *124*, 99–119. [CrossRef]
80. Allen, R.G.; Pereira, L.S.; Raes, D.; Smith, M. FAO Irrigation and drainage paper No. 56. *Rome Food Agric. Organ. United Nations* **1998**, *56*, e156.
81. De Kauwe, M.G.; Lin, Y.S.; Wright, I.J.; Medlyn, B.E.; Crous, K.Y.; Ellsworth, D.S.; Maire, V.; Prentice, I.C.; Atkin, O.K.; Rogers, A.; et al. A test of the 'one-point method' for estimating maximum carboxylation capacity from field-measured, light-saturated photosynthesis. *New Phytol.* **2016**, *210*, 1130–1144. [CrossRef]
82. Jiang, C.; Ryu, Y. Multi-scale evaluation of global gross primary productivity and evapotranspiration products derived from Breathing Earth System Simulator (BESS). *Remote Sens. Environ.* **2016**, *186*, 528–547. [CrossRef]
83. Houborg, R.; Anderson, M.C.; Norman, J.M.; Wilson, T.; Meyers, T. Intercomparison of a 'bottom-up' and 'top-down' modeling paradigm for estimating carbon and energy fluxes over a variety of vegetative regimes across the U.S. *Agric. For. Meteorol.* **2009**, *149*, 1875–1895. [CrossRef]
84. Bauerle, W.L.; Oren, R.; Way, D.A.; Qian, S.S.; Stoy, P.C.; Thornton, P.E.; Bowden, J.D.; Hoffman, F.M.; Reynolds, R.F. Photoperiodic regulation of the seasonal pattern of photosynthetic capacity and the implications for carbon cycling. *Proc. Natl. Acad. Sci. USA* **2012**, *109*, 8612–8617. [CrossRef] [PubMed]
85. Stinziano, J.R.; Huner, N.P.; Way, D.A. Warming delays autumn declines in photosynthetic capacity in a boreal conifer, Norway spruce (*Picea abies*). *Tree Physiol.* **2015**, *35*, 1303–1313. [CrossRef] [PubMed]
86. Bai, Y.; Shi, L.S.; Zha, Y.Y.; Liu, S.B.; Nie, C.W.; Xu, H.G.; Yang, H.Y.; Shao, M.C.; Yu, X.; Cheng, M.H.; et al. Estimating leaf age of maize seedlings using UAV-based RGB and multispectral images. *Comput. Electron. Agric.* **2023**, *215*, 108349. [CrossRef]
87. Adams, M.L.; Norvell, W.A.; Peverly, J.H.; Philpot, W.D. Fluorescence and reflectance characteristics of manganese deficient soybean leaves: Effects of leaf age and choice of leaflet. *Plant Soil* **1993**, *155–156*, 235–238. [CrossRef]
88. De Pury, D.G.G.; Farquhar, G.D. Simple scaling of photosynthesis from leaves to canopies without the errors of big-leaf models. *Plant Cell Environ.* **1997**, *20*, 537–557. [CrossRef]